



Multifunctional nanoparticles based on a polymeric copper chelator for combination treatment of metastatic breast cancer



Ping Zhou^{a,1}, Jiaqi Qin^{b,1}, Ce Zhou^b, Guoyun Wan^b, Yuanyuan Liu^b, Mingming Zhang^c, Xiaoying Yang^b, Ning Zhang^{a,**}, Yinsong Wang^{b,*}

^a Tianjin Medical University Cancer Institute and Hospital, National Clinical Research Center for Cancer, Key Laboratory of Cancer Prevention and Therapy of Tianjin, Tianjin's Clinical Research Center for Cancer, Tianjin, 300060, China

^b School of Pharmacy, Tianjin Key Laboratory on Technologies Enabling Development of Clinical Therapeutics and Diagnostics (Theranostics), School of Basic Medical Science, Tianjin Medical University, Tianjin, 300070, China

^c Institute of Biomedical Engineering, Chinese Academy of Medical Sciences & Peking Union Medical College, Tianjin, 300192, China

ARTICLE INFO

Keywords:

Multifunctional nanoparticles
Copper chelator
Antiangiogenesis
Immunotherapy
Breast cancer

ABSTRACT

Copper plays an important role in tumor growth and metastasis. Copper chelation has been confirmed to be an effective strategy for breast cancer therapy through antiangiogenesis. In this work, a copper chelating coil-comb block copolymer RGD-PEG-*b*-PGA-*g*-(TETA-DTC-PHIs) (RPTDH) was synthesized and used to prepare nanoparticles for loading resiquimod (R848), a TLR7 and TLR8 agonist, thus to combine antiangiogenesis and immune activation to treat breast cancer. RPTDH has strong copper-chelating ability and could self-assemble to form spherical nanoparticles with significant pH-sensitivity. R848 was efficiently loaded into RPTDH nanoparticles and exhibited greatly accelerated releases in weakly acid media simulating tumor microenvironment. RPTDH/R848 nanoparticles significantly inhibited the mobility, invasion and vascular tube formation of HUVECs via copper chelation, demonstrating their strong antiangiogenic activity in vitro. Furthermore, RPTDH/R848 nanoparticles remarkably induced the maturation and activation of human plasmacytoid dendritic CAL-1 cells, indicating their immune-activation ability. In breast tumor-bearing mice, RPTDH/R848 nanoparticles displayed excellent targeting ability for both primary breast tumor and lung metastases, and furthermore dramatically suppressed tumor growth and metastasis through copper deficiency-triggered antiangiogenesis and R848-induced immune activation. In summary, RPTDH/R848 nanoparticles can be used as an therapeutic agent against metastatic breast cancer through combining antiangiogenesis and immune activation.

1. Introduction

Breast cancer is one type of the most common cancer diagnosed among women and its incidence rates increased continually in recent years [1]. Copper levels are often elevated in breast cancer cells and copper is essential in cancer progression [2,3]. In 1980, McAuslan and Reilly found that copper salts are the simplest angiogenic components of tumor extracts [4]. Subsequent investigations showed that copper can stimulate endothelial cell proliferation and migration [5], and also is required for the secretion of several angiogenic factors by tumor cells [6,7]. Thus, inhibition of human copper trafficking can significantly attenuate the proliferation and motility of endothelial and cancer cells [8–10] and suppress tumor angiogenesis in animal models [11].

Targeting copper represents an effective strategy for breast cancer treatment [12]. Tetraethylomolybdate (TM), a copper chelator, has been confirmed to have powerful efficacy on suppression of angiogenesis and tumor growth through inducing copper deficiency [13], and is currently being tested in clinical trials. A woman involved in the trial, suffering from the “triple-negative” subclass of breast cancer, successfully survived and still exhibits no cancer signs after 8 years, likely due to the drug’s effects on antiangiogenesis and remodeling tumor microenvironment [14]. However, some unavoidable side effects of TM e.g., erythema, optic neuritis, emesis and leucopenia, have been observed in the treatments [15,16], probably resulting from nonselective copper removal from the whole body. Thus it can be seen that tumor-targeted delivery is very necessary for copper chelators as a novel kind of

* Corresponding author. Tianjin Medical University, Qixiangtai Road 22, Tianjin, 300070, China.

** Corresponding author. Tianjin Medical University Cancer Institute and Hospital, Huanhuxi Road, Tianjin, 300060, China.

E-mail addresses: zhangning@tmu.edu.cn (N. Zhang), wangyinsong@tmu.edu.cn (Y. Wang).

¹ P. Zhou and J. Qin contributed equally to this work.

angiogenesis inhibitors.

Tumor angiogenesis plays a crucial role in tumor growth and metastasis. However, antiangiogenesis treatments alone cannot enhance the overall survival of cancer patients and achieve robust and durable therapeutic effects [17]. Tumor immunosuppression is another crucial factor for tumor growth, invasion and metastasis. Over the last decade, cancer immunotherapies have emerged as a breakthrough for treatment of various types of cancer due to their clinical successes. Cancer immunotherapies mainly include immune checkpoint blockade, chimeric antigen receptor T cell therapies, tumor vaccines, cytokines and small-molecule immunoregulators. But unfortunately, these immunotherapies are only applicable to a subset of patients and some of them just exhibit transient effects [18,19]. Considering the important roles of angiogenesis and immunosuppression in cancer progress, antiangiogenesis in combination with immunotherapy has been brought forward recently and seems to be an effective strategy for cancer treatment [2]. Some clinical trials are currently under way to evaluate synergistic anticancer efficacy of antiangiogenic agents combined with immune checkpoint inhibitors [18,19]. However, so far as we know, few investigations have been conducted on the synergistic effects of copper chelator-induced antiangiogenesis and immunotherapy against breast cancer.

In this study, a polymeric copper chelator possessing tumor-targeting ability and pH-sensitivity is developed and used to prepare nanoparticles for tumor-targeted delivery and controlled release of resiquimod (R848), a Toll-like receptor (TLR) 7/8 agonist that has potent anti-tumor effects via activating dendritic cells (DCs) [20], thereby hoping to treat breast cancer more efficiently through combining copper chelation and immune activation. **Scheme 1A** illustrates the preparation of this multifunctional nanoparticle system. Triethylene-tetramine-bis(dithiocarbamate) (TETA-DTC), a specific copper chelator [21–23], was grafted onto poly- γ -glutamic acid (γ -PGA) via an amide bond. A pH-sensitive polymer, poly-L-histidine (PHis) [24], was introduced at the end amino group of TETA-DTC, and meanwhile Arg-Gly-Asp peptide (RGD)-conjugated poly(ethylene glycol) (RGD-PEG) was connected to γ -PGA through a highly acid-labile benzoic-imine bond [25,26], thus obtaining a coil-comb block copolymer RGD-PEG-*b*-PGA-*g*-(TETA-DTC-PHis) (RPTDH). In neutral and weak alkaline media, RPTDH can self-assemble to form nanoparticles due to aggregation of PHis segments via hydrophobic interaction and can therefore load hydrophobic R848. **Scheme 1B** shows the antitumor mechanisms of R848-loaded RPTDH (RPTDH/R848) nanoparticles. After intravenous injection, the nanoparticles are stable at physiological pH and can reach the targeted tumor through the enhanced permeation and retention (EPR) effect and specific binding of RGD peptide with integrin $\alpha v\beta 3$, which is often overexpressed on both neovasculature and tumors [27]. In a weakly acidic tumor microenvironment [28], these nanoparticles gradually destabilize and disintegrate due to the cleavage of benzoic-imine bond and the hydrophobic/hydrophilic transition of PHis segments, thus releasing R848 to activate DCs through the TLR 7/8-mediated signaling pathway [29,30]. The residual polymer, PGA-*g*-(TETA-DTC-PHis), further exerts its antiangiogenic and antitumor activities through copper chelation.

2. Materials and methods

2.1. Materials

γ -PGA with a molecular weight of approximately 100 kDa, produced through fermentation by *Bacillus subtilis*, was purchased from Shandong Freda Biotechnology Co., Ltd. (Shandong, China). The α -amino- ω -hydroxyl terminated poly(ethylene glycol) ($\text{NH}_2\text{-PEG-OH}$) with a molecular weight of 2000 was supplied by ZZBIO Co., Ltd. (Shanghai, China). The Fmoc-protected Arg-Gly-Asp peptide (Fmoc-RGD) and Fmoc-poly(L-histidine) (Fmoc-PHis) were synthesized by ChinaPeptides Co., Ltd. (Suzhou, China). Thiazolyl blue tetrazolium bromide (MTT), 4',6-diamidino-2'-phenylindole dihydrochloride

(DAPI) and IR780 iodide were purchased from Sigma-Aldrich (St Louis, MO, USA). All other chemical reagents were of analytical grade and obtained from commercial sources.

Human umbilical vein endothelial cell line (HUVEC) were purchased from Cell Culture Center of Chinese Academy of Medical Sciences (Beijing, China) and cultured in DMEM medium (Gibco, Life Technologies, USA) containing 10% fetal bovine serum (FBS), penicillin/streptomycin, endothelial cell growth supplement and heparin. To induce the angiogenesis of HUVECs, 1 μM of CuSO₄ was added to the culture medium. Normal lung epithelial BEAS-2B cells and breast cancer MCF-7, MDA-MB-231 and 4T1 cells were obtained from American Type Culture Collection, and luciferase-labeled 4T1 (4T1-Luc) cell line was purchased from Cold Spring Biotech Corp Company. These cells were cultured in DMEM medium containing 10% FBS and penicillin/streptomycin. pDC-like CAL-1 cells were gifted by Dr. De Yang from the Frederick National Laboratory for Cancer Research (Frederick, MD, USA) and cultured in RPMI 1640 medium supplemented with 10% FBS and 2 mM glutamine. The pH of culture medium was adjusted to be 6.5 and all cells were incubated at 37 °C in an atmosphere containing 5% CO₂.

Female BALB/c mice (5–6 weeks old) were purchased from the Food and Drug Verification Institute (Beijing, China). 4T1/4T1-Luc mouse models of breast cancer metastasis were constructed 4T1 or 4T1-Luc cells by injecting cells into the mammary fat pad of mice with 2×10^5 cells/mouse. All animal experiments were approved by the Animal Ethics Committee of Tianjin Medical University and complied with NIH guide for the care and use of laboratory animals.

2.2. Synthesis and characterization of RPTDH

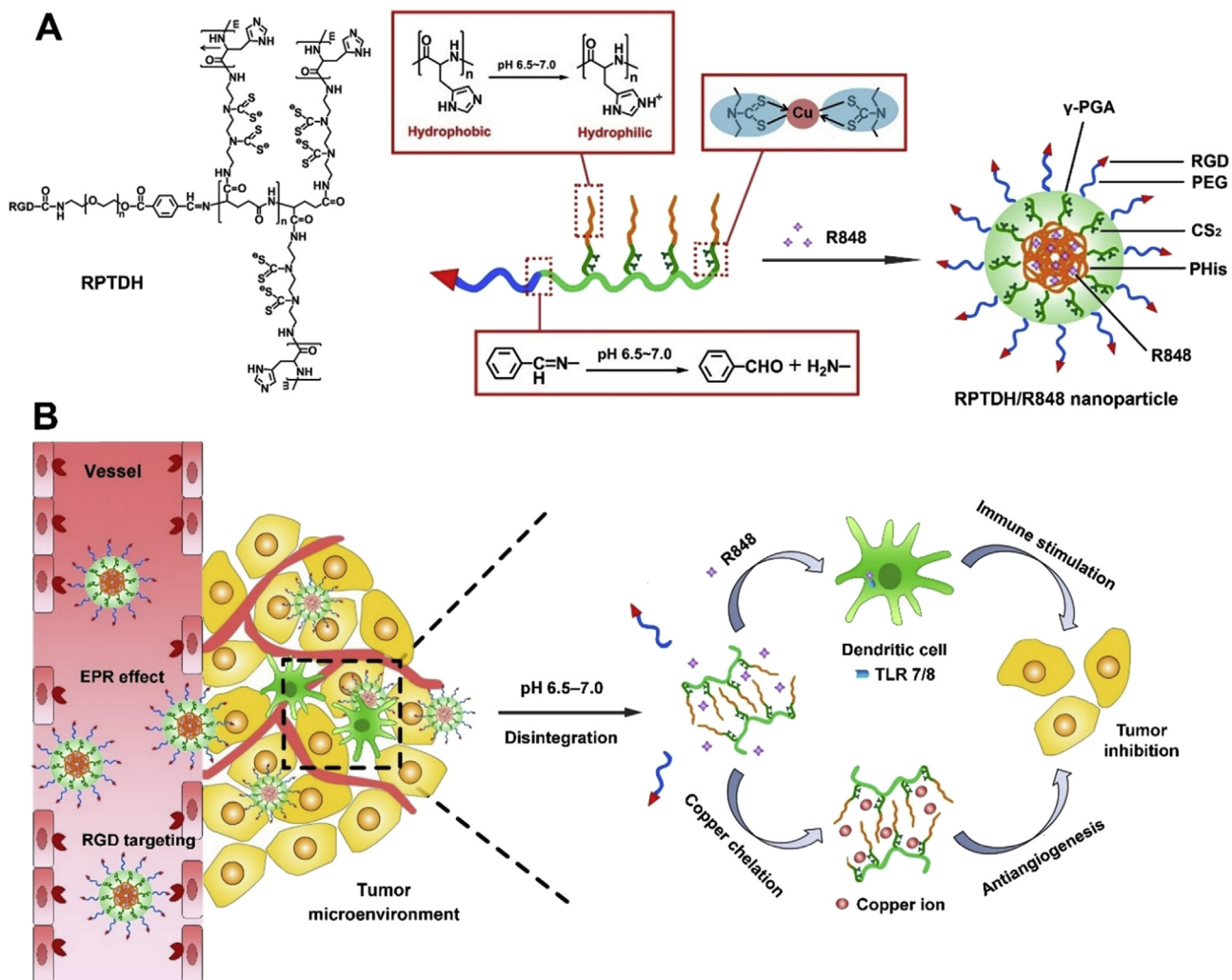
RPTDH was synthesized through a multistep process and chemically characterized using the Fourier transforming infrared spectroscopy (FT-IR), proton nuclear magnetic resonance (¹H NMR), inductively coupled plasma mass spectrometry (ICP-MS), and gel permeation chromatography (GPC). Furthermore, RGD-PEG-*b*-PGA-*g*-(TETA-PHis) (RPTH) without the copper-chelating DTC moiety was also synthesized for comparison. The synthesis routes and characterization of RPTDH and RPTH were detailedly described in the Supplementary data.

2.3. Evaluation of copper-chelating ability of RPTDH

The copper-chelating ability of RPTDH was first evaluated by the ultraviolet (UV) spectrometry. CuSO₄ (100 $\mu\text{mol/L}$) was mixed with RPTH or RPTDH (50 $\mu\text{g/mL}$) in phosphate buffered saline (PBS, pH 6.5), stirred at 100 rpm for 6 h, and then detected by a spectrometer (U-3310 UV, Hitachi, Tokyo, Japan) in the wavelength range from 190 nm to 300 nm. For comparison, the UV spectra of RPTH and RPTDH in PBS without adding CuSO₄ were also scanned at the same time. Furthermore, the copper-removal efficiency of RPTDH was measured using atomic absorption method. Briefly, RPTDH or RPTH at various concentrations in PBS (pH 6.5) were mixed with CuSO₄ (50 $\mu\text{mol/L}$) and stirred for 6 h, and then the mixtures were filtrated through the Amicon Ultra-4 centrifugal filters (Millipore, MWCO = 10 kDa). Subsequently, the copper concentrations in these filtrates were detected by a contrAA 700 atomic absorption spectrometry (Analytik Jena AG, German), and thus the copper-removal efficiencies could be calculated accordingly. Besides that, the chelating efficiencies of RPTDH for Fe²⁺, Mn²⁺ and Zn²⁺ were also detected using the same method to evaluate the selective chelating ability of RPTDH for Cu²⁺.

2.4. Preparation of RPTDH nanoparticles and in vitro evaluation of their pH-sensitivity

RPTDH nanoparticles were prepared using nanoprecipitation method. Briefly, 10 mg of RPTDH was dissolved in 1 mL of dimethyl formamide (DMF) and then added dropwise to 10 mL of borate buffer



Scheme 1. Schematic illustrations for preparation of RPTDH/R848 nanoparticles (A) and their functional mechanisms in breast cancer treatment (B).

(pH 7.6) under stirring, thus to form spherical nanoparticles by self-assembly. After lyophilization, RPTDH nanoparticles were resuspended in PBS with pH values of 7.4 and 6.5, and incubated for 30 min. During the whole incubation period, the morphologic changes of RPTDH nanoparticles were observed by a transmission electron microscopy (TEM, HT7700, Hitachi, Japan). After incubation, these nanoparticle solutions were filtrated through the Amicon Ultra-4 centrifugal filters (Millipore, MWCO = 30 kDa), lyophilized and finally characterized using an AMX 400 MHz spectrometer (Bruker, Germany).

2.5. Steady state fluorescence probe method

Pyrene was firstly purified by recrystallization in ethanol. Then it was dissolved in methanol at a concentration of approximately 10^{-4} mol/L and dried under nitrogen atmosphere. RPTDH nanoparticles dispersed in PBS at pH 6.5 and pH 7.4 were subsequently added and mixed thoroughly with pyrene under sonication for 30 min. The final concentration of pyrene in each sample solution was 10^{-6} mol/L, which was nearly equal to the solubility of pyrene in water at 22 °C [31,32]. Next, the emission spectra of pyrene in RPTDH nanoparticles at different pH values were recorded by a fluorescence spectrophotometer (RF-5301PC, Shimadzu, Japan). Pyrene in deionized water was also detected meanwhile.

2.6. Preparation and characterization of RPTDH/R848 nanoparticles

10 mg of RPTDH was mixed with R848 at a series of weight ratios in 1 mL of DMF, which was then added dropwise to 10 mL of borate buffer (pH 7.6) under stirring to form RPTDH/R848 nanoparticles. To remove the unloaded R848, these nanoparticles were ultrafiltrated through the Amicon Ultra-4 centrifugal filters (Millipore, MWCO = 10 kD), washed and resuspended in 10 mL of borate buffer. The morphologies of thus obtained nanoparticles were observed using the TEM, and their sizes, size distributions and zeta potentials were determined by a Nano-ZS90 Zetasizer analyzer (Malvern Instruments, UK).

The loading capability of RPTDH nanoparticles for R848 was measured using the ultra-high performance liquid chromatography method (UPLC). Briefly, the lyophilized powders of RPTDH/R848 nanoparticles were dissolved in 0.1 mol/L HCl under stirring and then poured into methanol to extract R848. After centrifugation at 6000 rpm for 30 min, the supernatants were collected, and the R848 contents were detected using an ACQ-BSM UPLC system (Waters, Milford, MA, USA). A C18 analytical column (50 mm × 2.1 mm, 1.7 μm) was used and column temperature was 37 °C. The detection wavelength was set at 246 nm. The mobile phase consisted of methanol/0.05 M KH₂PO₄/triethylamine (55/45/0.2, v/v/v, pH 3.0) and the flow rate was 0.2 mL/min. The loading content (LC) and encapsulation efficiency (EE) of R848 were finally calculated according to the following formulas.

$$\text{LC (\%)} = (\text{the mass of loaded R848} / \text{the total mass of RPTDH}) \times 100\%$$

nanoparticles) × 100%

EE (%) = (the mass of loaded R848 / the total mass of fed R848) × 100%

2.7. In vitro releases of R848

The in vitro releases of R848 from RPTDH/R848 nanoparticles at different pH values were evaluated by the dynamic dialysis method. In detail, 5 mg of RPTDH/R848 nanoparticles were dispersed separately in 50 mL of PBS at pH 6.0, pH 6.5, pH 7.0 and pH 7.4, and then placed in an SHK-02-I horizontal shaker (North TZ-Biotech Develop, Beijing, China) under shaking at 100 rpm at 37 °C. At designated time intervals, 50 µL of release media were taken out and meanwhile 50 µL of fresh release media were added. The amounts of released R848 in release media were finally measured by the UPLC method, as described above.

2.8. MTT assay

The in vitro cytotoxicities of RPTDH and RPTDH/R848 nanoparticles in HUVECs, 4T1, MCF-7, MDA-MB-231 and BEAS-2B cells were evaluated using the MTT assay. Briefly, the cells were seeded into 96-well plates and then incubated separately with RPTDH and RPTDH/R848 nanoparticles at various concentrations for 48 h. The MTT reagent was added to each well and further incubated for 4 h. Next, the culture medium was removed and 150 µL of dimethyl sulfoxide was then added to each well. After shaking for 30 s, the absorbance of each well at 490 nm was measured using a microplate reader (BioTek Epoch, Winooski, VT, USA).

2.9. Wound-healing assay

HUVECs were seeded into the 60 mm dishes at a density of 8×10^5 cells/well and incubated for 24 h to grow a monolayer. Next, a linear wound was created across the middle of the well surface using a pipette tip, and the cells were then incubated in serum-free media containing free R848 (30 µmol/L), RPTH (50 µg/mL), RPTDH (50 µg/mL) and RPTDH/R848 nanoparticles (50 µg/mL). At 0, 3, 6, 9 and 12 h, the wound widths from 6 defined field under an IX50 inverted microscope (Olympus, Tokyo, Japan) were quantified and the images were captured subsequently.

2.10. Transwell assay

HUVECs were seeded into the upper chambers coated with Matrigel matrix (BD Biosciences, MA, USA) at a density of 5×10^4 cells/well and then cultured in serum-free media containing free R848 (30 µmol/L), RPTH (50 µg/mL), RPTDH (50 µg/mL) and RPTDH/R848 nanoparticles (50 µg/mL). Then, the cells were allowed to migrate for 24 h toward the lower chambers filled with culture media containing 10% FBS. Next, the cells that migrated to the bottom side of the membranes were stained with 1% crystal violet and visually counted in 6 random fields using a computer-based microscopy imaging system.

2.11. Tube-formation assay

Free R848 (30 µmol/L), RPTH (50 µg/mL), RPTDH (50 µg/mL) and RPTDH/R848 nanoparticles (50 µg/mL) were separately mixed with Matrigel matrix (BD Biosciences, MA, USA). Afterwards, the mixed Matrigel solutions were added to the 48-well plates and then incubated successively on the ice for 10 min and at 37 °C for 1 h to allow solidification. Next, HUVECs in 200 µL serum-free DMEM containing 2×10^5 cells were seeded onto these matrices and further incubated for 9 h. Finally, 6 random fields in each well were imaged using a computer-based phase-contrast microscope (Olympus, Tokyo, Japan) and

the endothelial cell tubes were subsequently counted.

2.12. ELISA assay

HUVECs and MDA-MB-231 cells were seeded into the 60-mm dishes at a density of 1×10^6 cells per dish and cultured for 12 h. Then, the cells were incubated separately with free R848 (30 µmol/L), RPTH (50 µg/mL), RPTDH (50 µg/mL) and RPTDH/R848 nanoparticles (50 µg/mL) for 48 h. An aliquot of the cell culture supernatant was then removed and assayed for the expression levels of interleukin-1 alpha (IL-1 α), vascular endothelial growth factor (VEGF), interleukin-8 (IL-8) and matrix metalloproteinase-2 (MMP-2) by the ELISA kits (ABCclone Biotechnology co., Ltd., Wuhan, China) according to the manufacturers' instructions.

2.13. Western blotting analysis

HUVECs and MDA-MB-231 cells were seeded into the 60 mm dishes and incubated separately with free R848 (30 µmol/L), RPTH (50 µg/mL), RPTDH (50 µg/mL), and RPTDH/R848 nanoparticles (50 µg/mL) for 24 h. Then, the nuclear and cytoplasmic proteins were extracted using a Nuclear-Cytosol Extraction Kit (P1200, Applygen Technologies Inc, Beijing, China). After that, 20 µg of protein per sample was separated by 10% SDS-PAGE and transferred onto a PVDF membrane. Next, the membranes were incubated separately with primary antibodies against NF-κB(p65), histone-H3 (Santa Cruz Biotechnology, Dallas, TX, USA), and β-actin (Affinity Biosciences, Shanghai, China) overnight at 4 °C, and followed by incubation with horseradish peroxidase (HRP)-conjugated secondary antibody. Finally, the membranes were processed with a chemiluminescence reagent (Thermo Fisher Scientific, USA), and the chemiluminescent signals were detected by a gel documentation and image analysis system (G: Box Chemi XT, Syngene, Frederick, MD, USA).

2.14. Subcellular distribution of the transcription factor nuclear factor kappa B (NF-κB)

The immunofluorescence staining method was used to evaluate the nuclear translocation of NF-κB in HUVECs and MDA-MB-231 cells. Briefly, the cells were plated in 12-well plates containing sterile coverslips and incubated separately with free R848 (30 µmol/L), RPTH (50 µg/mL), RPTDH (50 µg/mL) and RPTDH/R848 nanoparticles (50 µg/mL) for 24 h. Subsequently, the cells were fixed with 4% paraformaldehyde, quenched with 50 mM NH₄Cl, permeabilized in 0.2% Triton X-100, and blocked in 3% bovine serum albumin. After that, the cells were stained with antibody against NF-κB (p65) (Santa Cruz Biotechnology, Dallas, TX, USA) and probed with an Alexa Fluor 568-conjugated secondary antibody (Invitrogen). The cell nuclei were then stained with DAPI. Next, the coverslips were sealed with ProLongTM Gold antifade reagent (Invitrogen) and photographed under a laser confocal scanning microscope (FV1000; Olympus, Tokyo, Japan).

2.15. qRT-PCR detection

CAL-1 cells were seeded into the 12-well plates and then incubated with free R848, RPTDH and RPTDH/R848 nanoparticles at the same R848 concentrations for 8 h. The total RNA was extracted using TRIzol® Reagent (Ambion, Life Technologies, USA). Next, cDNA was synthesized using a FastQuant RT kit (TIANGEN, Beijing, China) and analyzed by an ABI7500 RT-PCR System (Applied Biosystems, Foster City, CA, USA) and RT-PCR Master Mix (SYBR Green). The primers were used according to the previous report [33]. TNF-α (sense: 5'-GGC AAC CAC TAA GAA TTC AAA-3', antisense: 5'- TCT CCA GAT TCC AGA TGT CAG-3'); IFN-α (sense: 5'-TTA GGC TCA CCC ATT TCA ACC-3', antisense: 5'-CAC AGA GCA GCT TGA CTT GC-3'); IL-6 (sense: 5'-AAA TTC GGT ACA TCC TCG ACG G-3', antisense: 5'-GGA AGG TTC AGG TTG TTT TCT GC-

3'); IL-12p40 (sense: 5'-ACA AAG GAG GCG AGG TTC TAA-3', anti-sense: 5'-CCC TTG GGG GTC AGA AGA G-3'); GAPDH (sense: 5'-TGC ACC ACC AAC TGC TTA GC-3', antisense: 5'-GGC ATG GAC TGT GGT CAT GAG-3').

2.16. Flow cytometry analysis

CAL-1 cells were seeded into the 60-mm dishes and incubated separately with free R848, RPTDH and RPTDH/R848 nanoparticles at dose of 5 $\mu\text{mol/L}$ (according to R848) for 24 h. Then, the cells were collected, washed twice with PBS and resuspended in PBS. Afterwards, the cells were separately incubated with FITC-labeled anti-CD80 and anti-CD83 antibodies, and PerCP-labeled anti-CD86 antibody (eBioscience Inc., San Diego, CA, USA) in the dark for 30 min. Finally, the cells were washed with PBS and analyzed using a BD FACSVerser flow cytometer (BD Biosciences, San Jose, CA, USA).

2.17. Tissue distribution and tumor accumulation in breast cancer mice

RPTDH/IR780 nanoparticles were firstly prepared, in which IR780 was used as a near-infrared dye to evaluate tissue distributions and tumor accumulation of RPTDH nanoparticles. Next, free IR780 and RPTDH/IR780 nanoparticles were separately injected into 4T1 tumor-bearing mice via the tail vein. At 6 h and 24 h after administration, the main organs (liver, kidney, spleen and lung) and tumors were removed from these mice and then imaged using an IVIS in vivo imaging system (PerkinElmer, Waltham, USA). Moreover, the lungs removed from the mice were fixed with 4% formaldehyde, embedded in paraffin, and then stained with haematoxylin and eosin (H&E) for further histopathological observation.

2.18. Evaluation of antitumor and antimetastatic effects in breast cancer mice

4T1-Luc tumor-bearing mice were randomly divided into 4 groups with 7 mice per group and separately received treatments of saline (the control), RPTH/R848 mixture, RPTDH and RPTDH/R848 nanoparticles. All treatments were administered by intravenous injection once every 4 d for 5 consecutive times. The doses of RPTH and RPTDH were both 12 mg/kg and the R848 dose was 3.5 mg/kg. The tumor sizes and body weights of mice were continuously monitored during the treatment period. At 28 d after tumor implantation, 5 mice per group were intraperitoneally injected with D-Luciferin, and then the main organs (lung, liver, spleen, and kidney) were removed immediately for further observation under a Xenogen IVIS Imaging system. These organs were fixed with 4% formaldehyde, paraffin-embedded, and stained with H&E for histopathological observation.

2.19. Copper content detection

The blood samples were collected from the mice into heparin pre-treated tubes and then centrifuged at 3000 rpm for 10 min to obtain the plasma. The tumors randomly selected from four mice each group were homogenized and then centrifuged to obtain the supernates. Meanwhile, tissue fractions after centrifugation were also collected for the following experiment. After that, the plasma and the supernates from tumor homogenates were digested in 70% nitric acid at 80 °C for 12 h and dispersed in ultrapure water. Finally, the copper contents in all above samples were detected using an atomic absorption spectrometry.

2.20. Quantitative analysis of CD3 and CD8

Tissue fractions obtained from above tumor homogenates were digested with 1 mg/mL of Collagenase IV (Solarbio Technology, Beijing, China) in Krebs-Ringer buffer for 1 h at 37 °C and then filtered through a cell strainer (BD Falcon, Sparks, MD, USA) to obtain the cells. These

cells were resuspend in 40% Percoll buffer (Solarbio Technology, Beijing, China) and further centrifuged at 2000 rpm for 30 min to acquire the immune cells. Subsequently, these immune cells were double stained with CD3-FITC and CD8-PerCP-Cy5.5 (Invitrogen, Waltham, MA, USA) antibodies and subjected to flow cytometry analysis.

2.21. Immunohistochemical (IHC) staining

After the various treatments, 3 mice per group were sacrificed and the tumors were removed for further IHC analysis. Briefly, the paraffin-embedded tumor sections were mounted on slides, dewaxed in xylol and rehydrated in a graded ethanol series. Thus obtained slides were incubated in citrate buffer for antigen retrieval. These slides were processed separately with primary antibodies against CD31 (ab28364, Abcam, 1:100), CD3 (ab5690, Abcam, 1:200) and CD8 (ab203035, Abcam, 1:200) overnight at 4 °C, incubated with a secondary antibody of HRP/Fab polymer conjugated goat anti-rabbit IgG (PV-6001, ZSGB-BIO, Beijing, China, 1:1000) at 37 °C for 30 min, and finally observed under a fluorescence microscope.

2.22. Statistical analysis

All quantitative data are presented as the mean \pm standard deviation (SD) of at least three independent experiments. Statistical analysis of data was performed using the Student's t-test or one-way analysis of variance (ANOVA) in Graphpad Prism 6.02. The significance of difference was indicated as $P < 0.05$ or $P < 0.01$.

3. Results and discussion

3.1. Synthesis and copper-chelating ability of RPTDH

RPTDH was synthesized through a multistep process (Fig. S1). Some important intermediates and RPTDH were structurally characterized via FT-IR and $^1\text{H-NMR}$ (Figs. S2 and S3). The sulphur content of RPTDH determined by ICP-MS was $5.44 \pm 0.36\%$, which was similar to its theoretical value 5.24% (Table S1). The final molecular weight of RPTDH is 409 kDa as determined by GPC (Fig. S4). RPTH without the copper-chelating DTC moiety was also synthesized for comparison. The copper-chelating activity of RPTDH was evaluated using UV spectrometry and the results are shown in Fig. 1A. In the UV spectrum of RPTDH, the peaks that appeared at 207, 261 and 288 nm were assigned to the $n-\sigma^*$ transition of S=C=S group, the $\pi-\pi^*$ transition of the N=C=S group and the $\pi-\pi^*$ transition of the S=C=S group, respectively. After copper chelation, these three peaks red shifted separately to 213, 275 and 309 nm, which were generally consistent with another DTC-based polymeric copper chelator previously reported [21]. However, these characteristic absorption peaks were not observed in the UV spectra of RPTH both with and without chelating copper. We further assessed the copper-chelating efficiency of RPTDH after incubation with 50 $\mu\text{mol/L}$ of CuSO₄ for 6 h. Compared with RPTH, RPTDH exhibited a considerably increased copper-chelating efficiency and almost entirely removed copper ions in phosphate-buffered saline (PBS, pH 6.5) at a concentration greater than 50 $\mu\text{g/mL}$ (Fig. 1B). We also assessed the chelating abilities of RPTDH for Fe²⁺, Mn²⁺ and Zn²⁺. As shown in Fig. S5, RPTDH exhibited moderate removal efficiencies for Fe²⁺ and Mn²⁺, while very weak efficiency for Zn²⁺, which were basically consistent with the data of carbon disulfide reported previously [34]. These results demonstrated that RPTDH synthesized in this study had a strong and selective chelating ability for Cu²⁺.

3.2. Preparation, characterization and in vitro pH-sensitivity of RPTDH nanoparticles

RPTDH has pH-triggered hydrophobic/hydrophilic transition ability and displays distinct hydrophobic property in neutral and weak alkaline

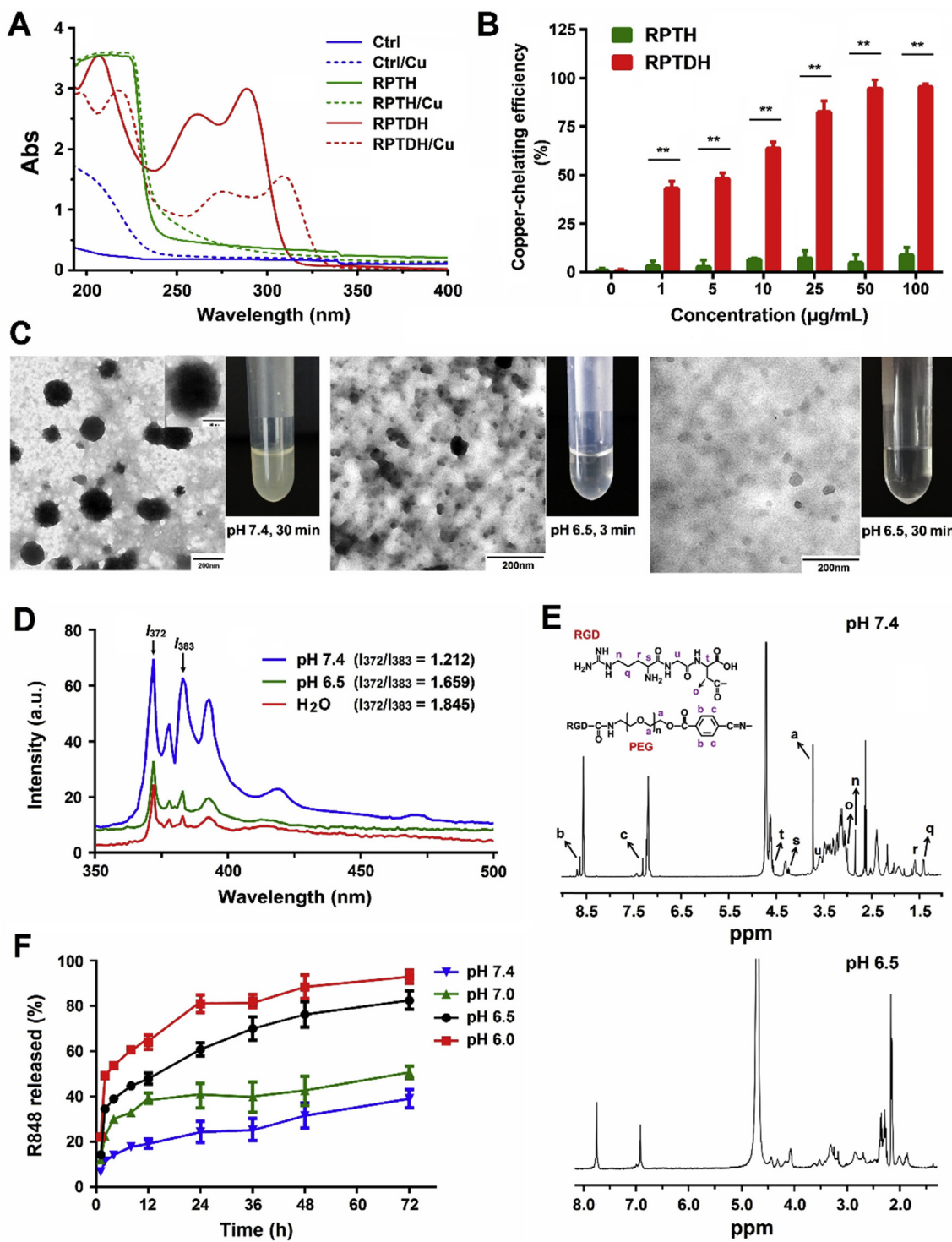


Fig. 1. Copper-chelating efficiency and pH-sensitivity of RPTDH nanoparticles. (A) UV spectra of RPTDH and RPTH with and without copper chelation. (B) Copper-chelating efficiencies of RPTDH and RPTH. ** $P < 0.01$ for comparison between two groups. (C) Morphological observations of RPTDH nanoparticles at pH 7.4 and pH 6.5. (D) Fluorescence spectra of pyrene in RPTDH nanoparticles at pH 7.4 and pH 6.5. (E) $^1\text{H-NMR}$ spectra of RPTDH nanoparticles after incubation at pH 7.4 and pH 6.5. (F) *In vitro* release profiles of R848 at different pH values.

media [24]. Thus RPTDH should possess amphiphilic characteristics due to the presence of both hydrophilic PEG-*b*-PGA backbone and hydrophobic PHis segments in its molecular structure, and can self-assemble to form nanoparticles in weak alkaline media through the aggregation of PHis segments. Here, we prepared RPTDH nanoparticles in pH 7.6 borate buffer using nanoprecipitation method. These nanoparticles had spherical shape with a size of approximately 200 nm (Figs. S6A and S6B). Owing to the hydrophobic-to-hydrophilic transition of

PHis segments, the disintegration of RPTDH nanoparticles will occur in acidic condition. To evaluate their pH-sensitivity, RPTDH nanoparticles were incubated in PBS at pH values of 7.4 and 6.5, and then their morphological and size changes were monitored continuously. At pH 7.4, RPTDH nanoparticles were very stable (Fig. S6C) and maintained a spherical shape; however, they gradually disintegrated at pH 6.5 and almost no particle morphology was observed after 30 min (Fig. 1C). Besides, the size and size distribution of RPTDH nanoparticles also

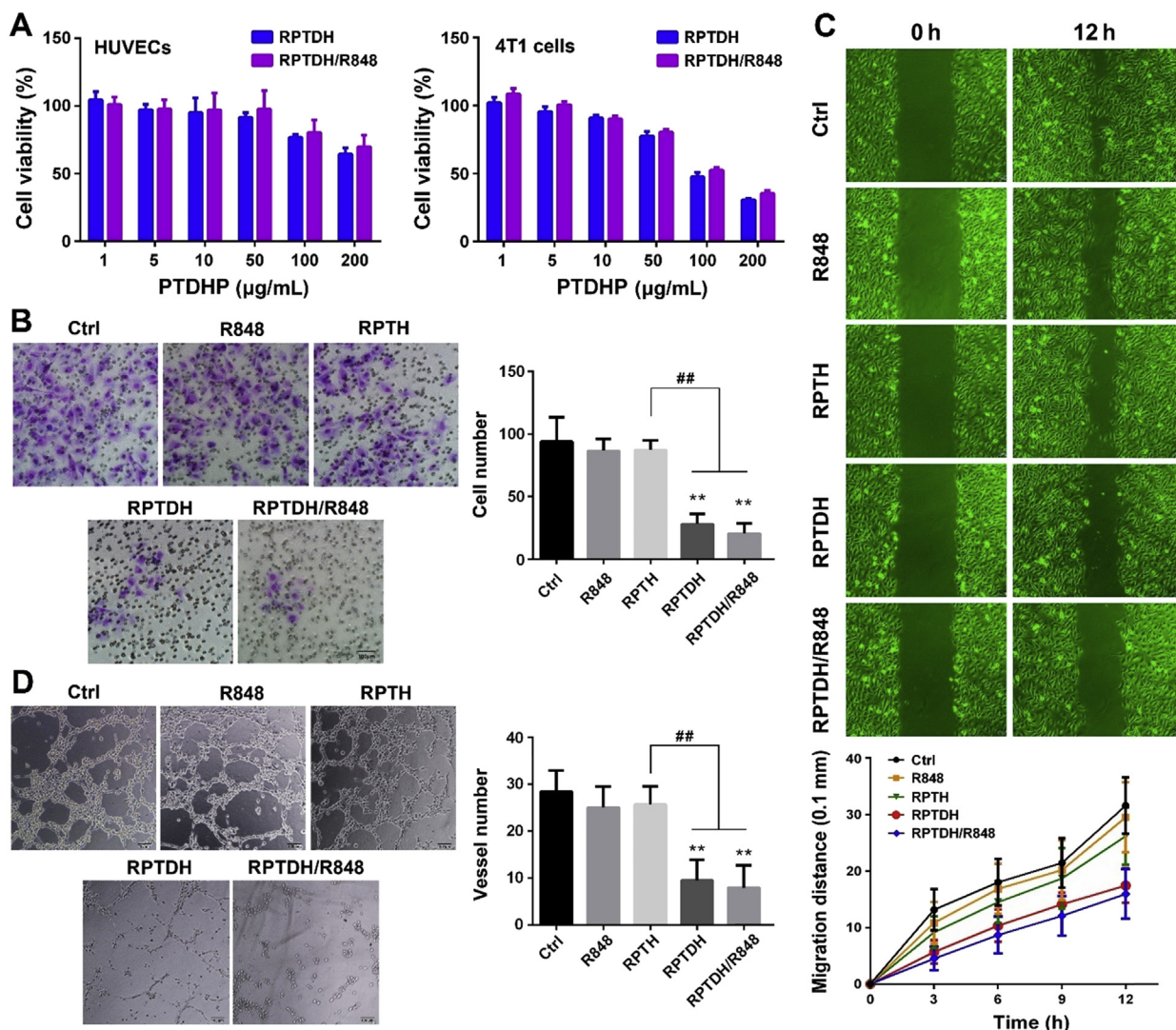


Fig. 2. In vitro effects of RPTDH/R848 nanoparticles. (A) Viabilities of HUVECs and 4T1 cells with 48-h treatments of RPTDH and RPTDH/R848 nanoparticles. Invasion (B), migration (C) and tube-formation abilities (D) of HUVECs treated with free R848, RPTH, RPTDH and RPTDH/R848 nanoparticles. ** $P < 0.01$ compared to the control; # $P < 0.01$ for comparison between two groups.

changed notably at pH 6.5 (Fig. S6D).

Next, we evaluated the structural stability of RPTDH nanoparticles at different pH values by a steady-state fluorescence probe method using pyrene as a probe. In microenvironments with different polarities, pyrene usually has different fluorescent characteristics. At concentrations lower than 10^{-5} mol/L, pyrene has five peaks appeared respectively at 372, 378, 383, 396, and 470 nm in its fluorescence spectrum, and the intensity ratio of the first peak at 372 nm to the third peak at 385 nm (I_{372}/I_{383}) is closely related to the polarity of its microenvironment [31,32]. The emission spectra of pyrene in deionized water and RPTDH nanoparticle solutions at pH 7.4 and 6.5 are shown in Fig. 1D. When the pH value decreased from 7.4 to 6.5, pyrene in RPTDH nanoparticles exhibited notably weakened fluorescence intensity and meanwhile the I_{372}/I_{383} value increased from 1.121 to 1.659, which was more close to that (1.845) in water. This finding meant that the pyrene microenvironment changed from hydrophobicity to hydrophilicity, which should be attributed to the hydrophobic/hydrophilic transition of PHis. In RPTDH, RGD-PEG was linked to γ -PGA through benzoic-imine bond, a pH-sensitive dynamic covalent bond that is stable at neutral pH, but starts to hydrolyze at an acidic pH of 6.5–7.0, corresponding to the mildly acidic extracellular environment of solid tumors [25,26]. We further assessed the pH-responsive-cleavage

capability of benzoic-imine bond in RPTDH nanoparticles using ^1H -NMR spectroscopy after 30-minutue incubation at pH 7.4 and pH 6.5. As shown in Fig. 1E, the characteristic proton signals of RGD-PEG segment at pH 7.4 almost completely disappeared at pH 6.5, indicating that the benzoic-imine bond between RGD-PEG and γ -PGA was successfully cleaved. All above results indicated that RPTDH nanoparticles possess distinct pH-sensitivity and can disintegrate under weakly acidic condition.

3.3. Drug loading capacity and pH-responsive drug release of RPTDH nanoparticles

Due to its strong hydrophobicity, R848 could be loaded into PHis self-assembled cores of RPTDH nanoparticles via hydrophobic interaction. To evaluate R848-loading capability of RPTDH nanoparticles, we prepared RPTDH/R848 nanoparticles with different weight ratios. The characteristic parameters of these nanoparticles are shown Table S2. When the weight ratio of R848/RPTDH was 4:10, RPTDH/R848 nanoparticles had a relatively high R848-loading content (18.8%) and encapsulation efficiency (47.7%), and their size and zeta potential were 225 nm and +23.6 mV, respectively. However, when the R848/RPTDH weight ratio was further increased to 5:10, the particle size increased

rapidly and the size distribution was widened markedly. Therefore, 4/10 was believed as an optimal weight ratio for preparing RPTDH/R848 nanoparticles and was used in our following experiments. The in vitro releases of R848 from RPTDH/R848 nanoparticles at different pH values were measured using dynamic dialysis method. The R848 release profiles are shown in Fig. 1F. Obviously R848 displayed an accelerated release rate when the pH of release medium decreased from 7.4 to 6.0. For example, more than 80% of R848 was released at pH 6.5 and 6.0 after 72 h, which was considerably higher than that at pH 7.4 and 7.0. This effect should be attributed to the rapid disintegration of RPTDH/R848 nanoparticles triggered by the hydrophobic/hydrophilic transition of PHis segments at acidic pH, according to the previous reports [26,35].

Given that solid tumors often exhibit acidic extracellular environment, we deduced that RPTDH/R848 nanoparticles would disintegrate in tumor microenvironment, thus leading to the release of R848 to exert the immune activation effects. Hence, we evaluated the disintegration of RPTDH/R848 nanoparticles in tumor stroma by detecting their size changes. As shown in Fig. S7, RPTDH nanoparticles maintained a relatively constant size in the plasma during 6-h storage, but obviously disintegrated within the same period and almost completely disappeared at 6 h. Next, we labeled RPTDH with fluorescein isothiocyanate (FITC) and prepared RPTDH-FITC/R848 nanoparticles, and then assessed their uptakes in tumor cells after incubation with tumor homogenate for different times using the flow cytometry. As shown in Fig. S8, RPTDH-FITC/R848 nanoparticles displayed significantly lower intracellular fluorescence signals as compared to free FITC at the same FITC concentrations, indicating that few nanoparticles were taken up by tumor cells. All these results suggested that RPTDH/R848 nanoparticles could disintegrate rapidly in the tumor microenvironment before their cellular internalization, which would be favorable for releasing R848 to exert the immune activation effects.

3.4. Cytotoxicity of RPTDH/R848 nanoparticles

MTT assay was used to evaluate the cytotoxicity of RPTDH and RPTDH/R848 nanoparticles in HUVECs and mouse breast cancer 4T1 cells after incubation for 48 h. Only when the concentration of RPTDH exceeded 100 µg/mL, RPTDH nanoparticles showed cytotoxicities on HUVECs and 4T1 cells to a certain extent, but a considerably higher inhibitory effect was observed in 4T1 cells (Fig. 2A). Besides, RPTDH nanoparticles also exhibited much higher cytotoxicity in human breast cancer MCF-7 and MDA-MB-231 cells than that in human normal lung epithelial BEAS-2B cells (Figs. S9A–S9C). This finding meant that copper-deficiency resulting from chelation of RPTDH can selectively inhibit the growth of cancer cells because of their requirement for more copper provision than normal cells. RPTDH/R848 nanoparticles displayed cytotoxicity almost identical to that of RPTDH nanoparticles in these cells, and free R848 showed no obvious cytotoxicity toward both HUVECs and 4T1 cells at a concentration less than 100 µmol/L (Fig. S9D). These results indicated that the cytotoxicity of RPTDH/R848 nanoparticles maybe mainly come from copper-chelation of RPTDH but not R848.

3.5. In vitro antiangiogenic effects of RPTDH/R848 nanoparticles

As previously reported, copper contributes to neovascularization via promoting the migration and invasion of endothelial cells [4]. Thus, 1 µmol/L of CuSO₄ was added to the culture medium to induce the angiogenesis in HUVECs in this study. As shown in Fig. S10, the addition of CuSO₄ only slightly promoted the migration, invasion and tube formation of HUVECs, which was probably because the culture medium itself contained a trace amount of copper ions. In view of the fact that cell migration and invasion are two critical factors affecting HUVEC cells to form tubes, we firstly evaluated the influence of RPTDH and RPTDH/R848 nanoparticles on the migration and invasion of HUVECs

using Transwell and wound healing assays. Compared with free R848 and RPTH, RPTDH and RPTDH/R848 nanoparticles both significantly inhibited the HUVEC invasion (Fig. 2B) and migration (Fig. 2C), indicating that copper-deficiency resulting from chelation of RPTDH can substantially influence the motility of HUVECs. Next, we further evaluated the influence of RPTDH and RPTDH/R848 nanoparticles on the tube formation ability of HUVECs using tube formation assay. The results are shown in Fig. 2D. In the control group and treatment groups of free R848 and RPTH, HUVECs formed evident tube-like networks in Matrigel-coated plates. However, their tube-forming ability was severely impaired by RPTDH and RPTDH/R848 nanoparticles e.g., most tubes remained open and an increased number of dissociative cells was also observed clearly. These results suggested that RPTDH and RPTDH/R848 nanoparticles have potent in vitro antiangiogenic efficacy due to their strong copper chelation ability.

3.6. Possible antiangiogenic mechanisms of RPTDH/R848 nanoparticles

IL-1α is a Cu²⁺-binding protein and its expression or release is often closely related to the intracellular copper level [36–38]. The transcription factor NF-κB is a crucial downstream effector of IL-1α and plays a vital role in regulating the expressions of genes important for cancer invasion, angiogenesis and metastasis. These genes include proangiogenic factors e.g., VEGF, IL-8, MMPs, and certain adhesion molecules [39]. Thus we further assessed the expressions of these signaling factors in both HUVECs and MDA-MB-231 cells to discuss possible antiangiogenic mechanisms of RPTDH/R848 nanoparticles. As shown in Fig. 3A, the IL-1α, VEGF, IL-8 and MMP-2 expressions detected by the ELISA kits were greatly reduced in HUVECs and MDA-MB-231 cells at 24 h after treatments of RPTDH and RPTDH/R848 nanoparticles. We also assessed the expressions of NF-κB in the nucleus and cytoplasm by western blotting analysis after subcellular fraction separation. As shown in Fig. 3B, the translocation of NF-κB from the cytoplasm to the nucleus was notably suppressed in HUVECs and MDA-MB-231 cells treated with RPTDH and RPTDH/R848 nanoparticles as compared to that with the control and other treatments, which can most likely be attributed to the copper chelation-induced reduction of IL-1α expression. The immunofluorescence technique was then used to observe the subcellular locations of NF-κB in HUVECs and MDA-MB-231 cells with different treatments. The confocal images also confirmed that the NF-κB nuclear translocation was markedly suppressed by RPTDH and RPTDH/R848 nanoparticles (Fig. 3C). From the above results, we deduced that it was the suppression of NF-κB nuclear translocation that down-regulated the expressions of VEGF, IL-8, and MMP-2 and further caused the inhibition of tumor angiogenesis. These results were basically consistent with antiangiogenic mechanisms of copper deficiency triggered by TM [39].

3.7. Maturation and activation of DCs induced by RPTDH/R848 nanoparticles

R848, an agonist for TLR 7/8, can stimulate antitumor immunity by mediating the maturation and activation of DCs through myeloid differentiation factor (MyD88)-dependent pathway [29,40,41]. In this study, RPTDH/R848 nanoparticles were prepared for combining antiangiogenesis and immune activation to treat breast cancer. Given that CAL-1 cells share many phenotypic and functions of human plasmacytoid DCs e.g., the expressions of TLRs (TLR7 and TLR9) and specific recognition for CpG motif-containing oligonucleotides, we evaluated the immune stimulation efficacy of RPTDH/R848 nanoparticles in CAL-1 cells. Upon activation through the TLRs/MyD88 signaling pathway, CAL-1 cells can secrete large amounts of type I interferons (IFNs) and certain pro-inflammatory cytokines, which are critical mediators bridging the innate and adaptive immune systems [33]. Here, we firstly detected the mRNA expression levels of IFN-α (a known type I IFN) and some pro-inflammatory cytokines including tumor necrosis factor-α

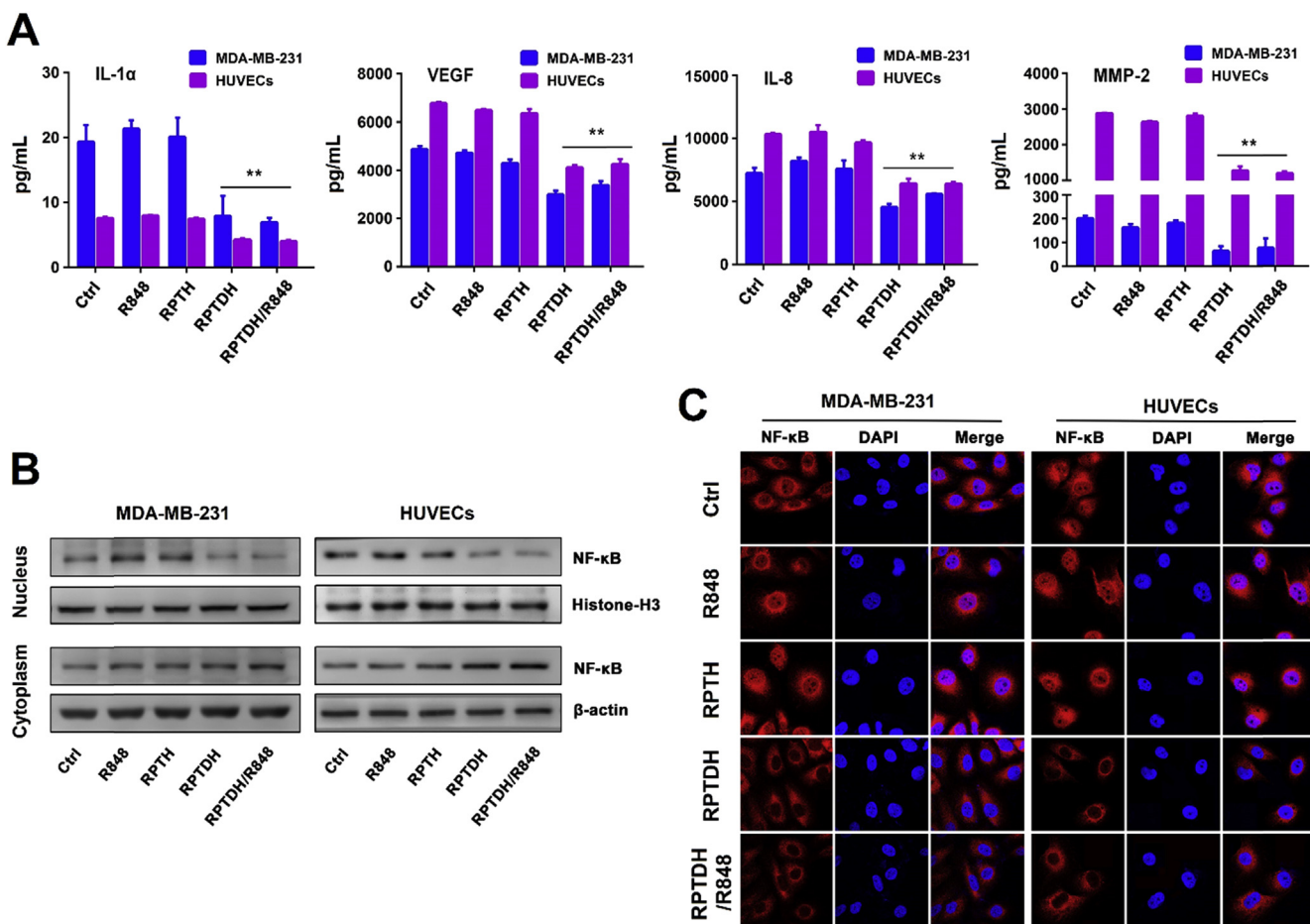


Fig. 3. Antiangiogenic mechanisms of RPTDH/R848 nanoparticles. (A) Protein expression levels of proangiogenic mediators including IL-1 α , IL-8, VEGF and MMP-2 in MDA-MB-231 cells and HUVECs detected by ELISA. **P < 0.01 compared to the control. (B) Protein expressions of NF-κB (p65) in nucleus and cytoplasm analyzed by Western blotting. (C) Subcellular locations of NF-κB (p65) observed by laser confocal microscope after immunofluorescence staining.

(TNF- α), IL-6 and IL-12p40 in CAL-1 cells after various treatments using quantitative real-time PCR (qRT-PCR). As shown in Fig. 4A, both free R848 and RPTDH/R848 nanoparticles substantially up-regulated the mRNA expressions of IFN- α , TNF- α , IL-6, and IL-12p40, demonstrating that these treatments induced the activation of CAL-1 cells. As previously reported [42], CD80 and CD86 are proteins expressed on DCs that provide costimulatory signals necessary for the activation, proliferation and survival of T cells, and CD83 is an important marker for the maturation of DCs. Hence, we further detected the protein expressions of CD80, CD86 and CD83 in CAL-1 cells using immunofluorescence technique. The results of flow cytometry showed that free R848 and RPTDH/R848 nanoparticles dramatically enhanced the CD80, CD86 and CD83 expressions in CAL-1 cells (Fig. 4B). These results confirmed that RPTDH/R848 nanoparticles have potent induction effect on the and activation of DCs, which were comparable to free R848.

3.8. Biodistribution of RPTDH/IR780 nanoparticles in breast cancer mice

IR780, a near-infrared dye, was loaded into RPTDH nanoparticles to prepare RPTDH/IR780 nanoparticles, which had spherical shape and almost identical size to RPTDH/R848 nanoparticles. An orthotopic mouse model of breast cancer was constructed by injecting 4T1 cells into the mammary fat pad of mice. These tumor-bearing mice were injected separately with free IR780 and RPTDH/IR780 nanoparticles through the tail vein at the same dose of IR780, and their main organs and tumors were then removed at 6 h and 24 h for further observation under an in vivo imaging system. Compared to free IR780, RPTDH/

IR780 nanoparticles changed tissue distributions of IR780 and notably enhanced its tumor accumulation in mice. At 24 h post injection, free IR780 was mainly located in the liver, kidney and tumor, whereas the fluorescence from RPTDH/IR780 nanoparticles was only observed in the lung and tumor (Fig. 5A). We further examined the pathological changes of lung tissues in these mice. As shown in Fig. 5B, the pulmonary metastases were clearly observed in the lung sections after H&E staining. These results demonstrated that RPTDH nanoparticles efficiently delivered IR780 to primary breast tumor and lung metastases, hereby confirmed their excellent tumor-targeting ability. We believed at least two factors were involved in breast cancer-targeted delivery of RPTDH nanoparticles. First, they can reach breast tumor and lung metastases through the EPR effect due to their nanometer size. Second, RGD peptide has specific affinity for integrin $\alpha v \beta 3$ expressed on both neovasculature and tumor cells [24], thus can mediate the efficient accumulation of RPTDH nanoparticles in the tumor microenvironment.

3.9. Antitumor effects of RPTDH/R848 nanoparticles in metastatic breast cancer mice

According to the previous report [43], 4T1-Luc cells were injected into the mouse mammary fat pad to construct a mouse model for metastatic breast cancer, which was used to evaluate the in vivo antitumor effects of RPTDH/R848 nanoparticles. All treatments were performed via intravenous injection every 4 d for 5 consecutive times. The doses of RPTH and RPTDH were both 12 mg/kg, and the R848 dose was 3.5 mg/kg. During the whole treatment period, the tumor growth and body weights of these mice were monitored. After treatments, the main

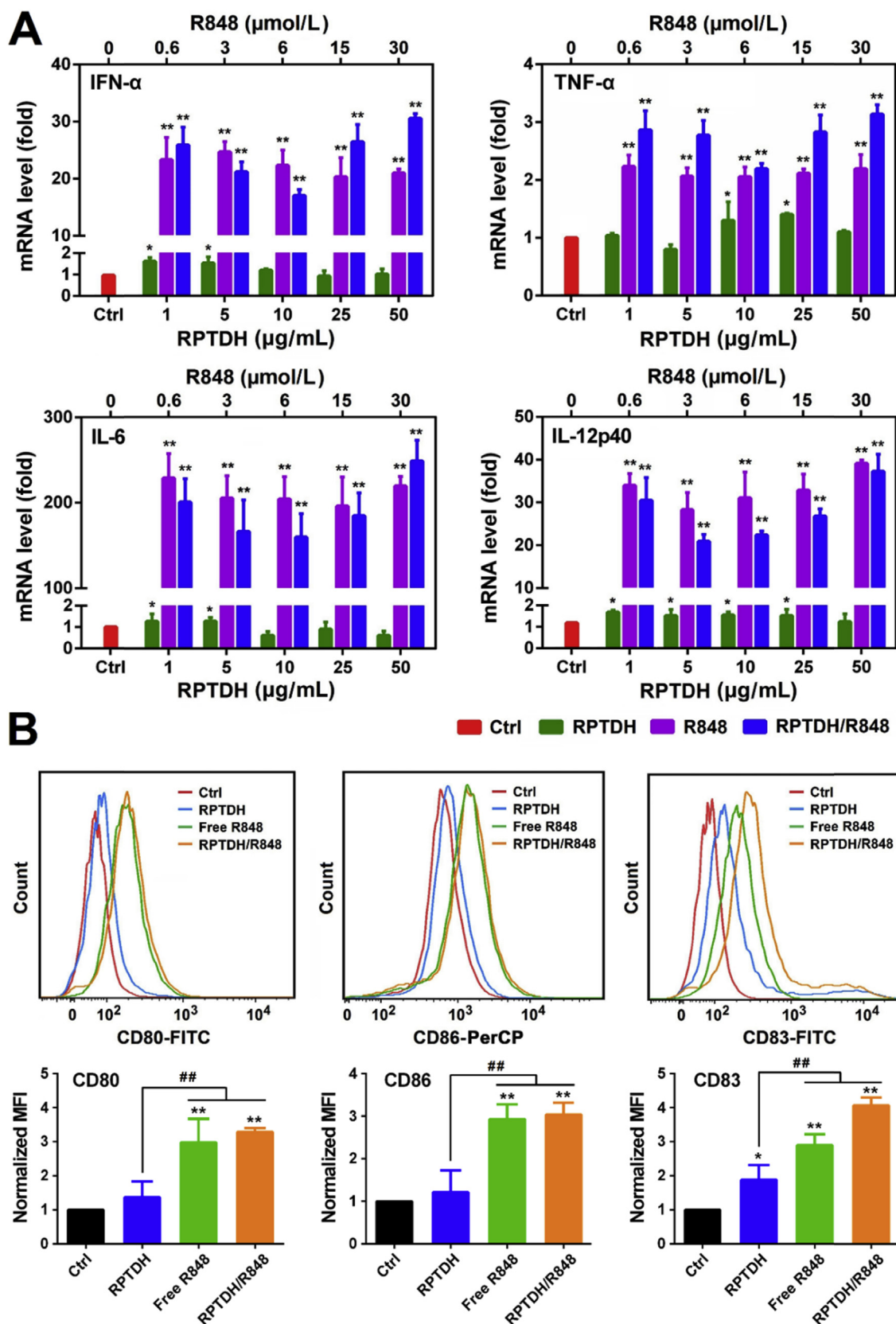


Fig. 4. In vitro effects of RPTDH/R848 nanoparticles on DC activation. (A) mRNA expression levels of IFN- α , TNF- α , IL-6, and IL-12p40 in CAL-1 cells treated with RPTDH, free R848 and RPTDH/R848 nanoparticles. (B) Flow cytometry analysis of CD80, CD86 and CD83 expressions in CAL-1 cells after various treatments. (C) Mean fluorescence intensities (MFIs) of CD80, CD86 and CD83 normalized to the control. * $P < 0.05$ and ** $P < 0.01$ as compared to the control; # $P < 0.01$ for comparison between two groups.

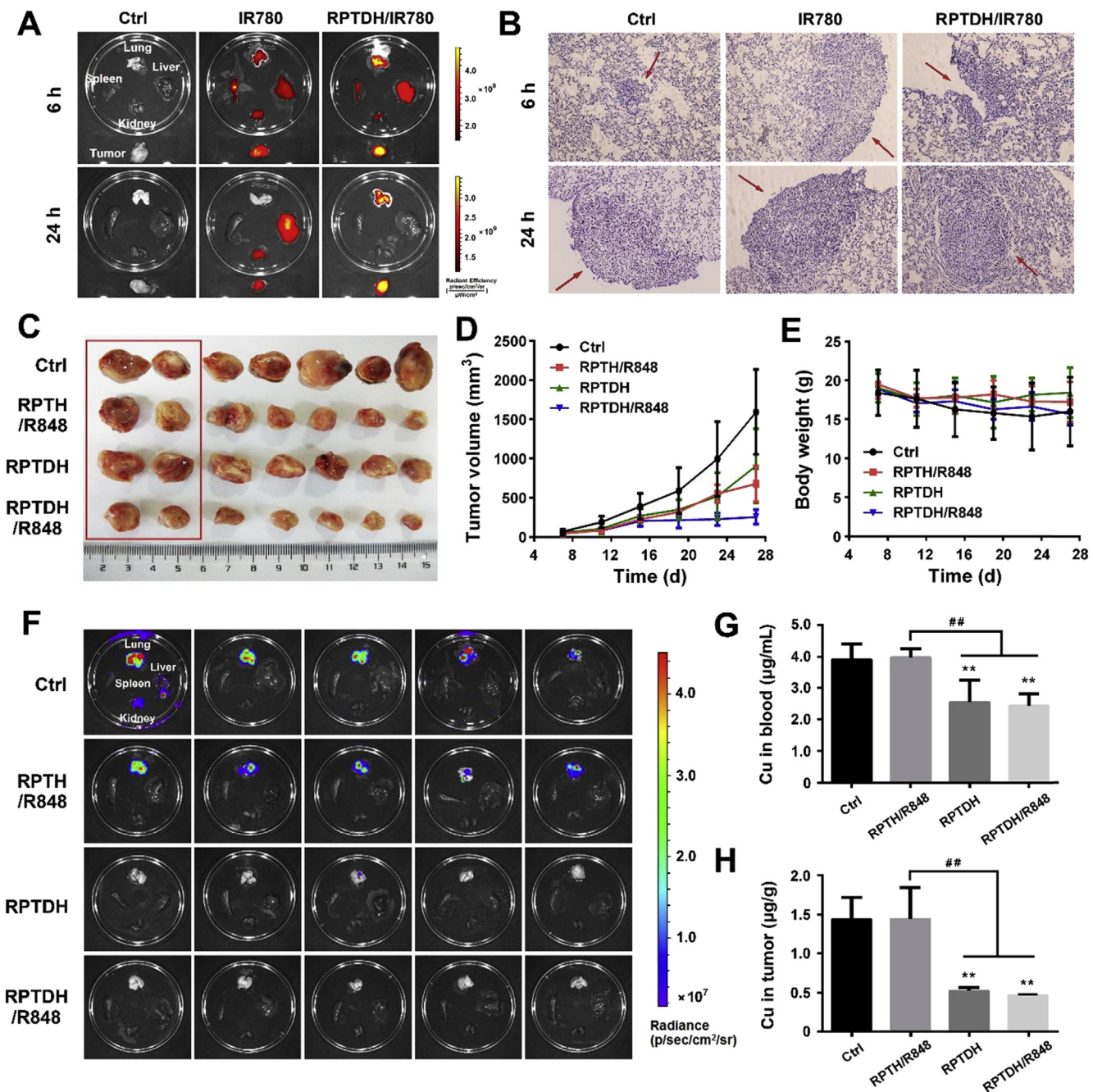


Fig. 5. Biodistribution and antitumor effects of RPTDH/R848 nanoparticles. (A) Fluorescence images of the main organs and tumors removed from 4T1 tumor-bearing mice after intravenous injection of free IR780 and RPTDH/IR780 nanoparticles. (B) Microscopic images of H&E-stained lung sections. Red arrows indicate the lung metastases. (C) Picture of 4T1-Luc tumors removed from the mice with treatments of RPTH/R848, RPTDH and RPTDH/R848 nanoparticles. Tumor growth curves (D) and body weight changes (E) of mice during treatments. (F) Bioluminescence images of the main organs and tumors removed from the mice. Copper levels in blood (G) and tumor (H) in mice after treatments. ** $P < 0.01$ compared to the control; # $P < 0.01$ for comparison between two groups. (For interpretation of the references to colour in this figure legend, the reader is referred to the Web version of this article.)

organs and tumors were removed for histopathological examination. Compared to the control, all treatments inhibited tumor growth to some extents, but RPTDH/R848 nanoparticles showed the most potent antitumor efficacy, as evidenced by the smallest tumor size (Fig. 5C) and slowest tumor growth rate (Fig. 5D). These results indicated that RPTDH/R848 nanoparticles had synergistic inhibitory effects on tumor growth through RPTDH-mediated copper chelation and R848-induced immunity promotion. The body weights of mice did not significantly change during the treatment period (Fig. 5E) and no visible histopathological injuries were found in the liver, kidney and spleen after treatments (Fig. S11), which confirmed that these treatments had no

obvious in vivo toxicity. After intraperitoneal injection of D-luciferin, the lung metastases of 4T1-Luc tumors were clearly observed in the control and RPTH/R848 nanoparticles-treated mice under an in vivo imaging system, but almost completely disappeared in the mice with treatments of both RPTDH and RPTDH/R848 nanoparticles (Fig. 5F). Hence, it can be deduced that RPTDH-mediated copper chelation plays an important role in inhibiting lung metastasis of breast tumor.

Next, the blood and tumor microenvironment levels of copper in mice after various treatments were detected using atomic absorption spectroscopy. RPTDH and RPTDH/R848 nanoparticles markedly reduced the copper levels in both blood (Fig. 5G) and tumors (Fig. 5H),

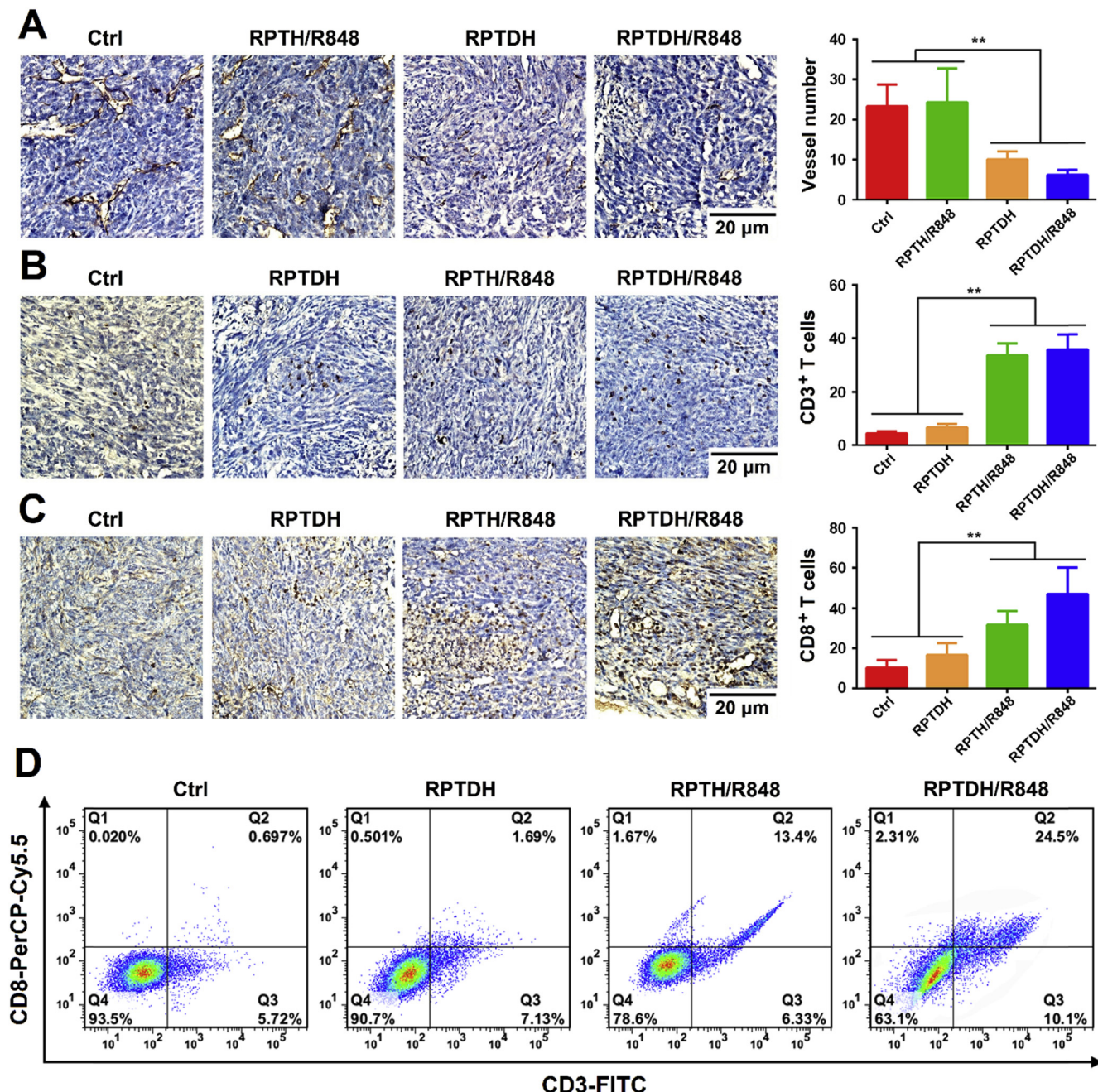


Fig. 6. Neovascularization and cytotoxic T cell infiltration in tumor. Microphotographs of tumor sections stained with anti-CD31 (A), anti-CD3 (B) and anti-CD8 antibodies (C), and the comparisons of vessel numbers, CD3⁺ and CD8⁺ T cells. (D) Flow cytometry analysis of CD3 and CD8 expressions on the immune cells obtained from tumors. **P < 0.01 for comparison between two groups.

whereas the similar copper removal effect was not found in mice treated with RPTH/R848 nanoparticles. Given that the copper-deficiency can suppress angiogenesis [11], we evaluated the tumor neovascularization by immunohistochemical staining with CD31 antibody. Compared to the control and RPTH/R848 nanoparticles, both RPTDH and RPTDH/R848 nanoparticles showed strong inhibitory effect on tumor angiogenesis, as evidenced by the disappearance of large vessels and significantly reduced microvessel densities (Fig. 6A). As a specific ligand for TRL7/8, R848 can stimulate DCs and subsequently induce the activation of cytotoxic T cells [44], which play a central role in cell-mediated antitumor immunity [39,45,46]. CD3 and CD8 are ideal markers for T cells and cytotoxic T cells, respectively, thus we further assessed the levels of tumor-infiltrating CD3⁺ and CD8⁺ T cells by IHC staining. Both RPTH/R848 and RPTDH/R848 nanoparticles notably

enhanced the infiltration of CD3⁺ T cells in tumors (Fig. 6B), and most of these accumulated T cells were activated as CD8⁺ T cells (Fig. 6C), demonstrating the activation of antitumor immunity. The immune cells were also isolated from the tumors, double-stained with CD3-FITC and CD8-PerCP-Cy5.5 antibodies and then analyzed by the flow cytometry. The results are shown in Fig. 6D. RPTH/R848 and RPTDH/R848 nanoparticles both enhanced the CD3 and CD8 expressions on the immune cells, confirming the accumulation and activation of T cells in tumor microenvironment. By contrast, RPTDH/R848 nanoparticles displayed much stronger effect on the activation of T cells. According to the investigation reported recently [39,45,46], we believed it was probably related to normalization of the abnormal tumor vasculature caused by angiogenesis. All results above demonstrated that RPTDH/R848 nanoparticles can greatly inhibit breast tumor growth and metastasis

through antiangiogenesis and immunotherapy.

4. Conclusion

In this study, a polymeric copper chelator RPTDH was synthesized and used to prepare nanoparticles possessing tumor-targeting ability and pH-responsive disintegration property for efficient loading, targeted delivery and controlled release of TRL7/8 agonist R848. Our preliminary data showed that RPTDH/R848 nanoparticles can suppress angiogenesis through RPTDH-induced copper deficiency and stimulate antitumor immunity via R848-triggered DC activation in tumor microenvironment, and thus effectively inhibit breast tumor growth and metastasis both in vitro and in vivo. In view of these facts, we deduced that RPTDH/R848 nanoparticles may be applied in the treatment of advanced and metastatic breast cancer.

Notes

The authors declare no competing financial interest.

Acknowledgments

This research was supported by the Natural Science Foundation of China (81573005, 81602724 and 81661128009), the Natural Science Foundation of Tianjin (18JCZDJC33400 and 17JCYBJC29100), the Tianjin Municipal 13th five-year plan (Tianjin Medical University Talent Project), and the Postgraduate Innovation Fund of '13th Five-Year comprehensive investment' of Tianjin Medical University (YJSCX201714).

Appendix A. Supplementary data

Supplementary data to this article can be found online at <https://doi.org/10.1016/j.biomaterials.2019.01.007>.

References

- [1] C. DeSantis, J. Ma, L. Bryan, A. Jemal, Breast cancer statistics, 2013, *CA Cancer J. Clin.* 64 (2014) 52–62.
- [2] A. Gupte, R.J. Mumper, Elevated copper and oxidative stress in cancer cells as a target for cancer treatment, *Cancer Treat Rev.* 35 (2009) 32–46.
- [3] H. Cai, F. Peng, Knockdown of copper chaperone antioxidant-1 by RNA interference inhibits copper-stimulated proliferation of non-small cell lung carcinoma cells, *Oncol. Rep.* 30 (2013) 269–275.
- [4] B.R. McAuslan, W. Reilly, Endothelial cell phagokinetics in response to specific metal ions, *Exp. Cell Res.* 130 (1980) 147–157.
- [5] G.F. Hu, Copper stimulates proliferation of human endothelial cells under culture, *J. Cell. Biochem.* 69 (1998) 326–335.
- [6] H. Xie, Y.J. Kang, Role of copper in angiogenesis and its medicinal implications, *Curr. Med. Chem.* 16 (2009) 1304–1314.
- [7] S.A. Lowndes, A.L. Harris, The role of copper in tumour angiogenesis, *J. Mammary Gland Biol. Neoplasia* 10 (2005) 299–310.
- [8] J. Wang, C. Luo, C. Shan, Q. You, J. Lu, S. Elf, Y. Zhou, Y. Wen, J.L. Vinkenborg, J. Fan, H. Kang, R. Lin, D. Han, Y. Xie, J. Karpus, S. Chen, S. Ouyang, C. Luan, N. Zhang, H. Ding, M. Merkx, H. Liu, J. Chen, H. Jiang, C. He, Inhibition of human copper trafficking by a small molecule significantly attenuates cancer cell proliferation, *Nat. Chem.* 7 (2015) 968–979.
- [9] H. Cai, J.S. Wu, O. Muzik, J.T. Hsieh, R.J. Lee, F. Peng, Reduced ^{64}Cu uptake and tumor growth inhibition by knockdown of human copper transporter 1 in xenograft mouse model of prostate cancer, *J. Nucl. Med.* 55 (2014) 622–628.
- [10] A.S. Fernandes, A. Flórido, N. Saraiva, S. Cerqueira, S. Ramalhete, M. Cipriano, M.F. Cabral, J.P. Miranda, M. Castro, J. Costa, N.G. Oliveira, Role of the copper(II) complex Cu[15]pyN5 in intracellular ROS and breast cancer cell motility and invasion, *Chem. Biol. Drug Des.* 86 (2015) 578–588.
- [11] A.K. Boal, A.C. Rosenzweig, Structural biology of copper trafficking, *Chem. Rev.* 109 (2009) 4760–4779.
- [12] D. Denoyer, S. Masaldan, S. La Fontaine, M.A. Cater, Targeting copper in cancer therapy: 'Copper that Cancer', *Metallooms* 7 (2015) 1459–1476.
- [13] H.M. Alvarez, Y. Xue, C.D. Robinson, M.A. Canalizo-Hernandez, R.G. Marvin, R.A. Kelly, A. Mondragón, J.E. Penner-Hahn, T.V. O'Halloran, Tetraethylomolybdate inhibits copper trafficking proteins through metal cluster formation, *Science* 327 (2010) 331–334.
- [14] K. Garber, Targeting copper to treat breast cancer, *Science* 349 (2015) 128–129.
- [15] G.J. Brewer, P. Hedera, K.J. Kluin, M. Carlson, F. Askari, R.B. Dick, J. Sitterly, J.K. Fink, Treatment of Wilson disease with ammonium tetrathiomolybdate: III. Initial therapy in a total of 55 neurologically affected patients and follow-up with zinc therapy, *Arch. Neurol.* 60 (2003) 379–385.
- [16] G.J. Brewer, Zinc and tetrathiomolybdate for the treatment of Wilson's disease and the potential efficacy of anticopper therapy in a wide variety of diseases, *Metallooms* 1 (2009) 199–206.
- [17] R.R. Ramjiawan, A.W. Griffioen, D.G. Duda, Anti-angiogenesis for cancer revisited: is there a role for combinations with immunotherapy? *Angiogenesis* 20 (2017) 185–204.
- [18] Y. Yang, Cancer immunotherapy: harnessing the immune system to battle cancer, *J. Clin. Invest.* 125 (2015) 3335–3337.
- [19] A. Lee, S. Sun, A. Sandler, T. Hoang, Recent progress in therapeutic antibodies for cancer immunotherapy, *Curr. Opin. Chem. Biol.* 44 (2018) 56–65.
- [20] T. Yin, S. He, Y. Wang, Toll-like receptor 7/8 agonist, R848, exhibits antitumoral effects in a breast cancer model, *Mol. Med. Rep.* 12 (2015) 3515–3520.
- [21] L. Lihua, W. Jun, L. Yulin, L. Xin, Z. Rongjin, Synthesis of a novel amphoteric chelating polymer flocculant and its performance in Cu^{2+} removal, *J. Appl. Polym. Sci.* 127 (2013) 2082–2094.
- [22] R. Tremmel, P. Uhl, F. Helm, D. Wupperfeld, M. Sauter, W. Mier, W. Stremmel, G. Hofhaus, G. Fricker, Delivery of copper-chelating trientine (TETA) to the central nervous system by surface modified liposomes, *Int. J. Pharm.* 512 (2016) 87–95.
- [23] H.Y. Cho, R.A. Blum, T. Sunderland, G.J. Cooper, W.J. Jusko, Pharmacokinetic and pharmacodynamic modeling of a copper-selective chelator (TETA) in healthy adults, *J. Clin. Pharmacol.* 49 (2009) 916–928.
- [24] H. Wu, L. Zhu, V.P. Torchilin, pH-sensitive poly(histidine)-PEG/DSPE-PEG copolymer micelles for cytosolic drug delivery, *Biomaterials* 34 (2013) 1213–1222.
- [25] Y. Akiyama, Y. Nagasaki, K. Kataoka, Synthesis of heterolechelic poly(ethylene glycol) derivatives having α -benzaldehyde and ω -pyridyl disulfide groups by ring opening polymerization of ethylene oxide using 4-(diethoxymethyl)benzyl alkoxide as a novel initiator, *Bioconjugate Chem.* 15 (2004) 424–427.
- [26] J. Gu, W. Cheng, J. Liu, S. Lo, D. Smith, X. Qu, Z. Yang, pH-triggered reversible "stealth" polycationic micelles, *Biomacromolecules* 9 (2008) 255–262.
- [27] S. Katsamakas, T. Chatzisideri, S. Thysiadis, V. Sarli, RGD-mediated delivery of small-molecule drugs, *Future Med. Chem.* 9 (2017) 579–604.
- [28] H.J. Li, J.Z. Du, J. Liu, X.J. Du, S. Shen, Y.H. Zhu, X. Wang, X. Ye, S. Nie, J. Wang, Smart superstructures with ultrahigh pH-sensitivity for targeting acidic tumor microenvironment: instantaneous size switching and improved tumor penetration, *ACS Nano* 10 (2016) 6753–6761.
- [29] H. Hemmi, T. Kaiho, O. Takeuchi, S. Sato, H. Sanjo, K. Hoshino, T. Horiuchi, H. Tomizawa, K. Takeda, S. Akira, Small anti-viral compounds activate immune cells via the TLR7 MyD88-dependent signaling pathway, *Nat. Immunol.* 3 (2002) 196–200.
- [30] M. Jurk, F. Heil, J. Vollmer, C. Schetter, A.M. Krieg, H. Wagner, G. Lipford, S. Bauer, Human TLR7 or TLR8 independently confer responsiveness to the antiviral compound R-848, *Nat. Immunol.* 3 (2002) 499.
- [31] P. Liu, S. Sun, X. Guo, X. Yang, J. Huang, K. Wang, Q. Wang, J. Liu, L. He, Competitive host-guest interaction between beta-cyclodextrin polymer and pyrene-labeled probes for fluorescence analyses, *Anal. Chem.* 87 (2015) 2665–2671.
- [32] K. Kalyanasundaram, J.K. Thomas, Environmental effects on vibronic band intensities in pyrene monomer fluorescence and their application in studies of micellar systems, *J. Am. Chem. Soc.* 99 (1977) 2039–2044.
- [33] Y. Liu, L. Qiao, S. Zhang, G. Wan, B. Chen, P. Zhou, N. Zhang, Y. Wang, Dual pH-responsive multifunctional nanoparticles for targeted treatment of breast cancer by combining immunotherapy and chemotherapy, *Acta Biomater.* 66 (2018) 310–324.
- [34] N. Burham, S. Abdel-Hafeez, S. Abdel-Azeem, M. El-Shahat, Retention profile of Fe, Mn and Cu onto chemically treated polyurethane with carbon disulfide, *Int. J. Environ. Anal. Chem.* 93 (2013) 1413–1427.
- [35] Y. Wang, H. Chen, Y. Liu, J. Wu, P. Zhou, Y. Wang, R. Li, X. Yang, N. Zhang, pH-sensitive pullulan-based nanoparticle carrier of methotrexate and combretastatin A4 for the combination therapy against hepatocellular carcinoma, *Biomaterials* 34 (2013) 7181–7190.
- [36] A. Mandinova, R. Soldi, I. Graziani, C. Bagala, S. Bellum, M. Landriscina, F. Tarantini, I. Prudovsky, T. Maciag, S100A13 mediates the copper-dependent stress-induced release of IL-1alpha from both human U937 and murine NIH 3T3 cells, *J. Cell Sci.* 116 (2003) 2687–2696.
- [37] F. Suska, M. Esposito, C. Gretzer, M. Kalltorp, P. Tengvall, P. Thomsen, IL-1alpha, IL-1beta and TNF-alpha secretion during *in vivo/ex vivo* cellular interactions with titanium and copper, *Biomaterials* 24 (2003) 461–468.
- [38] L. Mandinov, A. Mandinova, S. Kyurkchiev, D. Kyurkchiev, I. Kehayov, V. Kolev, R. Soldi, C. Bagala, E.D. de Muinck, V. Lindner, M.J. Post, M. Simons, S. Bellum, I. Prudovsky, T. Maciag, Copper chelation represses the vascular response to injury, *Proc. Natl. Acad. Sci. U. S. A.* 100 (2003) 6700–6705.
- [39] Q. Pan, C.G. Kleer, K.L. van Golen, J. Irani, K.M. Bottema, C. Bias, M. De Carvalho, E.A. Mesri, D.M. Robins, R.D. Dick, G.J. Brewer, S.D. Merajver, Copper deficiency induced by tetrathiomolybdate suppresses tumor growth and angiogenesis, *Cancer Res.* 62 (2002) 4854–4859.
- [40] A. Gabrielson, Y. Wu, H. Wang, J. Jiang, B. Kallakury, Z. Gatalica, S. Reddy, D. Kleiner, T. Fishbein, L. Johnson, E. Island, R. Satoskar, F. Banovac, R. Jha, J. Kachhela, P. Feng, T. Zhang, A. Tesfaye, P. Prins, C. Loffredo, J. Marshall, L. Weiner, M. Atkins, A.R. He, Intratumoral CD3 and CD8 T-cell densities associated with relapse-free survival in HCC, *Cancer Immunol. Res.* 4 (2016) 419–430.
- [41] T. Yin, S. He, Y. Wang, Toll-like receptor 7/8 agonist, R848, exhibits antitumoral effects in a breast cancer model, *Mol. Med. Rep.* 12 (2015) 3515–3520.
- [42] J.S. Pufnock, M. Cigal, L.S. Rolczynski, E. Andersen-Nissen, M. Wolf, M.J. McElrath, P.D. Greenberg, Priming CD8⁺ T cells with dendritic cells matured using TLR4 and TLR7/8 ligands together enhances generation of CD8⁺ T cells

- retaining CD28, *Blood* 117 (2011) 6542–6551.
- [43] J. Kalra, M. Anantha, C. Warburton, D. Waterhouse, H. Yan, Y.J. Yang, D. Strut, M. Osooly, D. Masin, M.B. Bally, Validating the use of a luciferase labeled breast cancer cell line, MDA435LCC6, as a means to monitor tumor progression and to assess the therapeutic activity of an established anticancer drug, docetaxel (Dt) alone or in combination with the ILK inhibitor, QLT0267, *Cancer Biol. Ther.* 11 (2011) 826–838.
- [44] Y. Liu, L. Qiao, S. Zhang, G. Wan, B. Chen, P. Zhou, N. Zhang, Y. Wang, Dual pH-responsive multifunctional nanoparticles for targeted treatment of breast cancer by combining immunotherapy and chemotherapy, *Acta Biomater.* 66 (2018) 310–324.
- [45] H.R. Ali, E. Provenzano, S.J. Dawson, F.M. Blows, B. Liu, M. Shah, H.M. Earl, C.J. Poole, L. Hiller, J.A. Dunn, S.J. Bowden, C. Twelves, J.M. Bartlett, S.M. Mahmoud, E. Rakha, I.O. Ellis, S. Liu, D. Gao, T.O. Nielsen, P.D. Pharoah, C. Caldas, Association between CD8⁺ T-cell infiltration and breast cancer survival in 12,439 patients, *Ann. Oncol.* 25 (2014) 1536–1543.
- [46] Y. Kwak, J. Koh, D.W. Kim, S.B. Kang, W.H. Kim, H.S. Lee, Immunoscore encompassing CD3⁺ and CD8⁺ T cell densities in distant metastasis is a robust prognostic marker for advanced colorectal cancer, *Oncotarget* 7 (2016) 81778–81790.